

Plasma-Enhanced Atomic Layer Deposition of HfO₂ on Monolayer, Bilayer, and Trilayer MoS₂ for the Integration of High- κ Dielectrics in Two-Dimensional Devices

Katherine M. Price,^{†,‡,§} Sina Najmaei,[‡] Chinedu E. Ekuma,^{‡,§} Robert A. Burke,[‡] Madan Dubey,[‡] and Aaron D. Franklin^{*,†,||}

[†]Department of Electrical and Computer Engineering, Duke University, Durham, North Carolina 27708, United States

[‡]Sensors and Electron Devices Directorate, United States Army Research Laboratory, Adelphi, Maryland 20783, United States

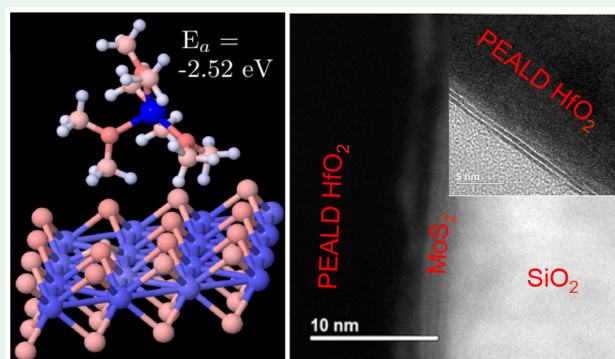
[§]Department of Physics, Lehigh University, Bethlehem, Pennsylvania 18015, United States

^{||}Department of Chemistry, Duke University, Durham, North Carolina 27708, United States

S Supporting Information

ABSTRACT: As two-dimensional (2D) electronic devices continue to advance, the need for integrating high-quality, high- κ nanoscale dielectrics becomes more essential. Plasma-enhanced atomic layer deposition (PEALD) is a promising approach for depositing ultrathin dielectrics directly onto the surface of 2D materials. However, the mechanism for PEALD film growth on the van der Waals materials, along with the impact of the plasma process on structural and interfacial properties of 2D materials, has not been fully explored. In this work, we demonstrate the effects of the plasma process on monolayer, bilayer, and trilayer MoS₂. Back-gated MoS₂ transistors of varying thickness were tested before and after ALD/PEALD HfO₂, and it was verified that plasma damage does occur, predominantly in the surface layer of the MoS₂, leading to significantly greater impact in monolayers. By increasing the thickness of the MoS₂, the adverse effects of the plasma process are reduced appreciably. This observation is further supported by Raman and transmission electron microscopy analysis. In addition to providing information about defect generation and morphology, this study provides key insights into the charge transfer between HfO₂ and MoS₂. Overall, this detailed analysis of the impact of the PEALD plasma process on MoS₂ contributes to the reliable integration of ultrathin, high- κ dielectrics in 2D devices.

KEYWORDS: two-dimensional electronic devices, high- κ nanoscale dielectrics, plasma enhanced atomic layer deposition, monolayer, bilayer, trilayer, MoS₂, HfO₂, 2D transistor, dielectric nucleation



Recent advances in the study of two-dimensional (2D) crystals, including molybdenum disulfide (MoS₂), have increased interest in the applications and integration of these layered materials. 2D crystals have shown great promise in a range of applications, from high-performance field-effect transistors (FETs) to flexible optoelectronics.^{1–6} The 2D nature of MoS₂ (a transition metal dichalcogenide (TMD)) is a result of its unique crystal structure and bonding properties. The crystal structure consists of a Mo layer sandwiched between two S layers arranged in a hexagonal lattice, where the intralayer atoms are strongly bound by covalent forces and weak interlayer van der Waals forces bring the individual layers together to form bulk MoS₂.⁷ These binding properties make it possible to isolate a monolayer via mechanical exfoliation or direct layer-by-layer growth.⁸ Because of the atomically thin planar geometry, dielectric screening in 2D devices plays a central role in determining the functionality; hence, the ability to effectively integrate oxides with 2D materials is an important

aspect of any technological advancement.^{9–11} The growth of thin, high-quality, and high- κ dielectrics on 2D crystals requires a concerted effort to develop deposition processes that are non-damaging to the underlying crystal and produce suitable interfaces between the 2D crystal and high- κ dielectric.

In principle, on certain substrates, ALD is a powerful layer-by-layer deposition technique with precise atomic control on the stoichiometry of the dielectric and complex oxide stacks (Figure 1c).¹² However, research has shown that 2D crystals are far from the ideal substrates for ALD growth due to their inert basal plane.^{13,14} The sparse density of nucleation sites results in island growth on the 2D surface that leads to continuous films only when a sufficiently thick layer is

Received: March 18, 2019

Accepted: July 1, 2019

Published: July 16, 2019

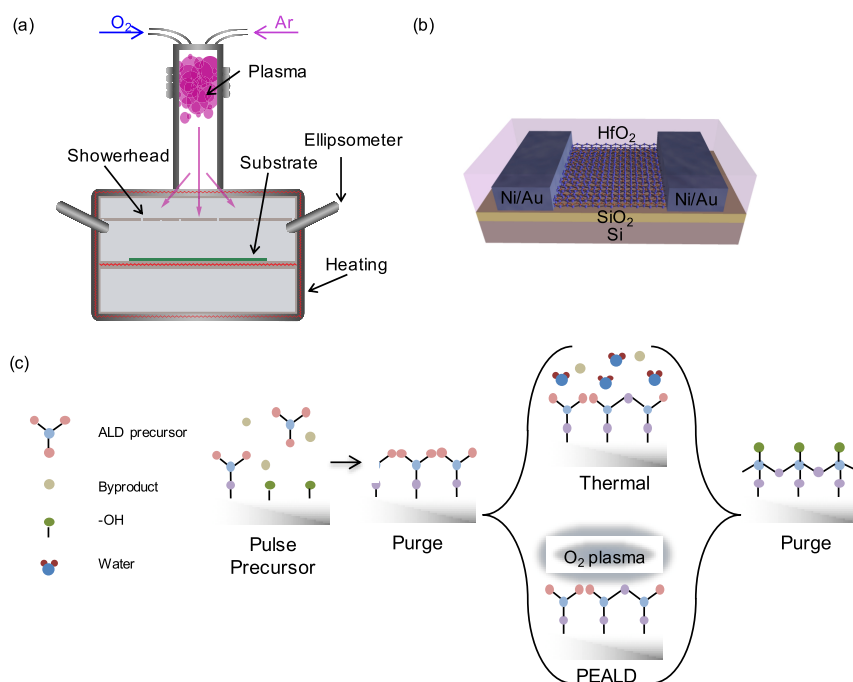


Figure 1. Schematics illustrating the (a) ALD/PEALD reaction chamber, (b) the final device structure, and (c) the ALD/PEALD reaction process.

deposited (>15 nm).^{1,3,15} Some proposed approaches to enhance nucleation on 2D surfaces include surface modification procedures and buffer layers, but these suffer from interfacial integrity, reliability, and scalability.^{16,17,26,18–25} Therefore, finding other means of controlled nucleation and growth in the ALD process is needed. Recently, plasma-enhanced atomic layer deposition (PEALD) has been shown to yield ultrathin (<5 nm) high- κ dielectric (e.g., HfO_2) film growth on MoS_2 .²⁷ While these results showed promise for devices of relatively thick 2D crystals (>7 nm), there has been no exploration of how PEALD impacts single or few-layer MoS_2 . Furthermore, an understanding of how the PEALD process is affecting the properties of the underlying MoS_2 , including the different impact on the topmost layer versus underlying layers, remains to be explored.

In this work, we used PEALD to deposit HfO_2 on monolayer, bilayer, and trilayer MoS_2 and examined the properties of the HfO_2 – MoS_2 system using electrical characterization, photoluminescence (PL), Raman spectroscopy, transmission electron microscopy (TEM), and first-principles calculations. The PEALD process used was the same as that used in ref 27, which includes details, such as its conformal nature on MoS_2 and absence of any detectable formation of MoO_3 , of the PEALD HfO_2 film on MoS_2 . By comparing the electrical characteristics of back-gated FETs before and after ALD and PEALD HfO_2 deposition (Figure 1b), we examined the interfacial changes and their effect on device performance. While significant degradation of the device performance was observed in monolayer samples, we noticed systematic improvement as the layer thickness is increased. Additionally, we used PL and Raman measurements to gain a more detailed understanding of the interfacial properties between the MoS_2 and PEALD HfO_2 . First-principles calculations were also used to explore the role of interfacial or subsurface O-vacancy. Our data suggest that O-vacancy as small as 0.90% induces a significant charge transfer from the HfO_2 substrate to the MoS_2 monolayer. These results

show that while the PEALD process is an excellent method for the growth of ultrathin high- κ dielectrics on relatively thick 2D crystals, better control of defects and interfacial quality is needed to adapt this growth approach to few-layer crystals.

METHODS

Chemical Vapor Deposition (CVD) MoS_2 Growth. MoS_2 triangular domains were grown on SiO_2/Si substrates by atmospheric pressure powder vaporization. Prior to growth, the substrates were cleaned in a piranha solution for 15 min followed by 5 min soaks in deionized (DI) water, acetone, and isopropyl alcohol. Afterward, 40 μ L of perylene-3,4,9,10-tetracarboxylic acid tetrapotassium salt (PTAS) was spin coated on each sample as a seeding layer for the growth. MoO_3 powder (18–20 mg) was added to an alumina boat, and four PTAS-coated substrates were placed on top of the alumina boat facing up with a 1.2 mm gap between each sample. The boat was loaded into the center of the furnace. The sulfur precursor (15–17 mg) was loaded in another alumina boat and placed in a region outside of the furnace where the temperature could be independently controlled by a heating tape. The growth process was performed in a tube furnace at a sample temperature of 750 °C and sulfur temperature of 250 °C. The growth was carried out for 10 min during which argon (5 sccm) was used as a carrier gas. After the growth was complete, the tube furnace was opened and the argon flow rate was increased to 200 sccm to quench the growth process.

ALD and PEALD HfO_2 Growth. ALD and PEALD were carried out in the same Kurt J. Lesker tool (model number ALD 150-LX) (Figure 1a). After initial electrical/Raman/PL characterization either ALD or PEALD HfO_2 was deposited onto the samples. Tetrakis-(dimethylamido)hafnium(IV) (TDMAH) was used as the Hf precursor and either H_2O vapor or O_2 plasma was used as the oxidant for thermal or plasma-enhanced ALD, respectively. For ALD HfO_2 the process had the following step times: 0.25 s pulse precursor/15 s purge/0.4 s pulse oxidant/15 s purge. PEALD HfO_2 had the following step times: 0.25 s pulse precursor/6 s purge/5 s pulse oxidant/5 s purge. The purge gas is 99.999% pure Ar, and the O_2 in the remote plasma has a purity of 99.999%. Both reactions were carried out at 120 °C, and the PEALD process was carried out at 400 W. Note, the plasma is upstream and does not have line-of-sight access to the substrate; rather, the plasma radicals flow through a showerhead structure to the growth substrate. The growth per cycle

(GPC) for PEALD HfO₂ is 0.13 nm/cycle and for ALD HfO₂ it is 0.12 nm/cycle. The number of cycles was variant upon the experiment. For the devices, 250 cycles of ALD/PEALD were deposited, and for the Raman and PL measurements, 42 cycles were deposited.

Device Fabrication. A grid was fabricated onto the untransferred CVD MoS₂ using a Vistec EBPG5000+ES electron beam lithography (EBL) system and CHA e-Beam Vacuum Evaporator System (EVAP) of Ti/Au. First, PMMA 950 A4 was spin coated onto MoS₂, and EBL was used to define the MoS₂ channel. After EBL, the chip was developed using a mixture of MIBK and IPA and then reactive ion etching was used to etch away the surrounding MoS₂. The remaining resist was removed using hot (80 °C) acetone. Next, the contact regions were defined using EBL and then EVAP was used to deposit the 50 nm Ni/50 nm Au contacts. The samples were left overnight under high vacuum in the EVAP, and the EVAP process was carried out at $\sim 3 \times 10^{-6}$ Torr. In order to remove the remaining resist, the samples were left in hot acetone overnight (Figure 1b).

Electrical Characterization. Devices were tested before and after ALD/PEALD HfO₂. After ALD, the contacts were probed through the ALD/PEALD HfO₂. All measurements were done under high vacuum in order to avoid interactions that could be dominated by surface adsorbates, such as water. The electrical characterization was carried out using a Keithley 4200 parameter analyzer.

Computational Approach. First-principles electronic structure calculations were performed using density functional theory (DFT) with planewave basis set as implemented in the *Vienna Ab Initio Simulation Package*.^{28,29} The calculations were done using the Perdew–Burke–Ernzerhof exchange–correlation functional. In constructing the MoS₂–HfO₂ slab, we used the monoclinic phase of HfO₂. The monoclinic phase of HfO₂ is not only the most energetically stable at ambient conditions but also provides a natural hexagonal surface along its 111-direction. For the computations, we assume a crystalline HfO₂; however, in reality it is most likely amorphous. The MoS₂–HfO₂ interface is studied by constructing an S-terminated MoS₂ and O-terminated HfO₂ (111) surface to form a periodically repeated slab separated by a vacuum of 25 Å. For the adsorption of TDMAH on MoS₂, the periodic images of the slabs were separated by ~ 15 Å. The HfO₂ part of the slab is composed of 56 Hf and 112 O atoms, which is thick enough to support the MoS₂ layer of 25 Mo and 50 S atoms. The slabs were fully relaxed until the energy (charge) is converged to within $\sim 10^{-4}$ (10^{-7}) eV and the forces dropped to $\sim 10^{-3}$ eV/Å. The optimization is done by sampling the Brillouin zone at the Γ -point. During the relaxation the ionic positions were allowed to move while keeping the volume of the cell constant. All calculations included van der Waals interactions and dipole corrections. At equilibrium pristine structure, the MoS₂ lies 2.93 ± 0.2 Å above the HfO₂ surface while the TDMAH sits at approximately 3.20 Å above the MoS₂ surface. For the defect structures, the above distances reduced by approximately 0.5 Å. We observed no covalent bonds on the defect-free MoS₂–HfO₂ interface. The MoS₂–HfO₂ slab has an in-plane distance of 15.915 Å leading to a lattice mismatch of $\sim 1.1\%$. The small strain in the slab did not change the location of the energy bandgap of MoS₂, which only decreased by ~ 0.04 eV and remained direct at the K-point of the high symmetry of the first Brillouin zone. In both the MoS₂–HfO₂ and the MoS₂–TDMAH hybrid structures, the MoS₂ monolayer crystal remained unperturbed with insignificant change in the bond lengths and lattice constant.

Raman and PL. Raman and PL were carried out in a WITec Alpha 300RA system. The measurements were carried out at liquid N₂ temperatures (~ 72 K) using a 532 nm laser at a power of 1 mW in the backscattering configuration. The spectra were measured using a 63 \times objective and a grating of 1800 grooves/mm. Raman spectra were acquired before and after 42 cycles of ALD/PEALD HfO₂ and were normalized to the A_{1g} peak. The Raman conditions were shown not to damage the MoS₂ as shown in Figure S7.

TEM and STEM. The TEM and STEM were conducted in a JEM 2100 FE-TEM. The operating voltage was 200 kV and the point-to-point resolution is ~ 0.2 nm.

RESULTS AND DISCUSSION

Effect of PEALD Plasma on Monolayer MoS₂ FETs.

The interfaces between different regions of field-effect devices play an important role in determining their electronic properties.³⁰ Interfacial effects are even more important in 2D van der Waals structures because poor screening induces stronger interfacial Coulombic scattering and more susceptibility to surface impurities.³¹ As a result, the design and optimization of interfaces in 2D FETs, such as the dielectric/channel material interface, is critical to the success of 2D device development.

PEALD is a plasma-enhanced process for deposition of extremely thin dielectrics (Figure 1c). The highly reactive properties of the plasma species at the deposition surface enables a greater level of control on materials processing, such as enabling lower growth temperatures and a greater variety of films that can be deposited when compared to traditional thermal ALD.³² This is precisely the reason that plasma-enhanced processes are explored for ultrathin oxide deposition on 2D crystals.²⁷ One drawback of PEALD is the potential for destructive interactions between the high-energy plasma radicals and the 2D crystal surface. To examine the impact of the plasma process on MoS₂, we designed a series of experiments on different thicknesses of MoS₂ and characterized the corresponding changes in the electrical properties of resultant 2D FETs.

The PEALD and ALD HfO₂ layer affect monolayer MoS₂ FETs (Figure 2a) differently, as shown in the representative transfer curves (Figure 2b and c). In order to achieve uniform coverage of MoS₂ with both ALD and PEALD films, 250 cycles of ALD/PEALD were deposited. Both films are assumed to be pinhole free due to their thickness, and previous research that has shown these films to be pinhole free even when considerably thinner (ref 27). The ALD HfO₂ encapsulation of the MoS₂ device strongly shifts the threshold voltage (V_t) to the left and reduces the hysteresis while maintaining the on-current (I_{on}) (Figure 2b). The shift in V_t can be attributed to n-type doping of MoS₂, as it takes a larger negative voltage to turn off the device. Due to the strong n-doping observed in our transfer characteristics, it is assumed that the ALD HfO₂ is oxygen deficient, causing it to be a charged film that influences the carrier density in the channel and contact regions.³³ These oxygen-dominated vacancy defect states in the HfO₂ can have occupied states that line up with the conduction band of MoS₂, thus doping the underlying MoS₂ leading to an electron-rich sample.^{34–36} In addition, the reduction in hysteresis could be due to the ALD HfO₂ acting as a protective passivation layer to ward off unstable adsorbates. These results confirm the effects of the HfO₂ layer on the electrical properties of MoS₂ and, as expected, the ALD process preserves the quality of the 2D crystal.

The 2D-FETs with ALD HfO₂ are used as a baseline to determine the influence of PEALD processing on MoS₂. Similar to the reference thermal ALD results, the hysteresis in the PEALD HfO₂-encapsulated MoS₂ devices was reduced (Figure 2c). However, in contrast to the reference devices, a pronounced degradation in I_{on} , shift in V_t and a rise in the p-branch is clearly discernible in the PEALD 2D-FETs indicating possible p-doping. These changes support the hypothesis that the plasma-enhanced process modifies the underlying MoS₂ crystal. It also could indicate that the PEALD HfO₂ is more electron rich compared to thermal ALD HfO₂. An increase in

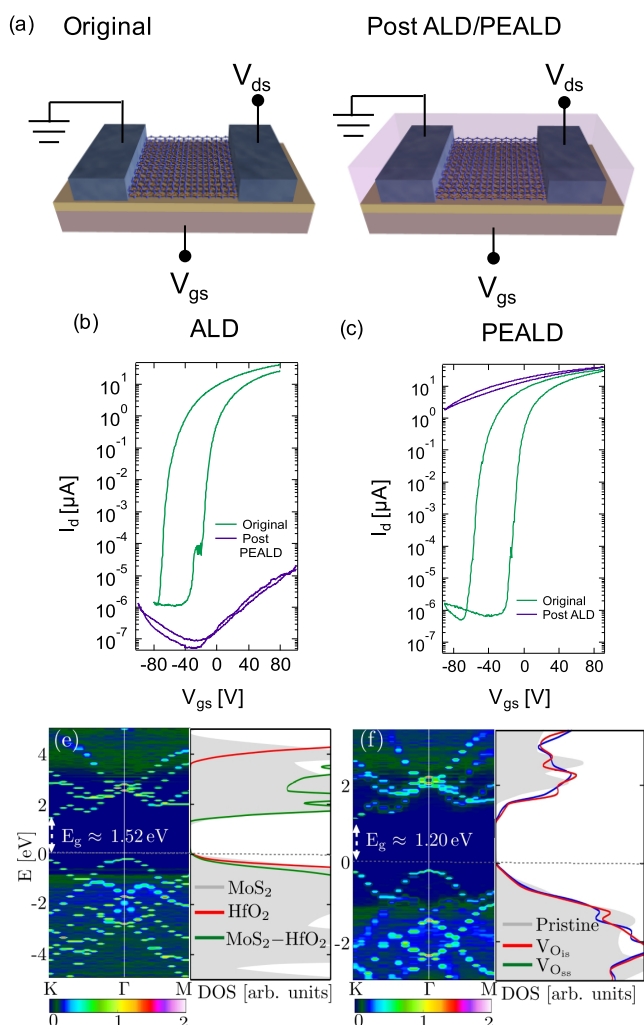


Figure 2. ALD versus PEALD HfO₂ growth on back-gated, monolayer MoS₂ devices. (a) Schematic of back-gated MoS₂ devices showing how they are tested before/after dielectric deposition. Subthreshold curves of monolayer MoS₂ before/after (b) ALD HfO₂ ($W = 1.0 \mu\text{m}$, $V_{\text{ds}} = 1.0 \text{ V}$, $L_{\text{ch}} = 0.9 \mu\text{m}$) and (c) PEALD HfO₂ ($W = 1.0 \mu\text{m}$, $V_{\text{ds}} = 1.0 \text{ V}$, $L_{\text{ch}} = 0.9 \mu\text{m}$). The electronic band structure, obtained from DFT calculations, unfolded onto the first Brillouin zone of monolayer MoS₂ and the associated density of states for (d) pristine crystals and (e) crystals with interfacial O-vacancy. The deposition of HfO₂ on MoS₂ leads to a negligible change in the bandgap of MoS₂, while either interfacial V_{O_{is}} or subsurface V_{O_{ss}} O-vacancies induce a decrease of $\sim 0.32 \text{ eV}$ in the bandgap. The horizontal dashed line is the Fermi level, which is set at the zero energy scale.

the scattering centers at the MoS₂–HfO₂ interface as a result of plasma damage can directly explain the degradation of the on-state conductivity in the devices. We hypothesize that the accompanied V_{t} shift and rise of the p-branch are also due to defect formations. One possibility is the formation of Mo–O bonds which have been shown to p-dope MoS₂, although this possibility is questionable due to no formation of MoO₃ being found in the XPS of ref 27 which used the same process as used here. Defects in the vicinity of the metal contacts can induce band bending and Fermi level pinning, both of which can modify the contact barrier characteristics. The band bending and Fermi level pinning supersede the doping effects seen in the ALD devices and dominate the V_{t} shifts.

First-Principles Calculations. In order to test our hypothesis and gain further understanding of the role of the plasma process on the MoS₂–HfO₂, we carried out first-principles calculations on the monolayer MoS₂–HfO₂ interface using density functional theory (DFT) [see Figure S1 in the Supporting Information (SI) for the structures] and experimentally examined the device characteristics of samples made on bilayer and trilayer MoS₂.

The electronic band structure and the density of states obtained for the pristine structures are shown in Figure 2d. The pristine slab shows the absence of covalent bonds and negligible charge transfer (CT) as could be inferred from the difference of the electron localization function (see Figure S1c in the SI). This could be understood from the more than 1.0 eV band offset for both the conduction and valence bands of HfO₂ and MoS₂, respectively. The absence of intrinsic potential difference and the large band offset creates a barrier for any charge transfer. The pristine electronic structures reveal a small change in the bandgap of monolayer MoS₂–HfO₂ interface. Herein, we focus on the states in the proximity of the bandgap. The valence band maximum is formed by the hybridization of MoS₂ (mainly from Mo-4d and S-3p states) and HfO₂ (O-2p states) while the conduction band maximum is derived predominantly from the Mo-4d states of MoS₂ monolayer. To model the defect structures, we constructed a MoS₂–HfO₂ slab with one missing oxygen atom from the interface V_{O_{is}} and subsurface V_{O_{ss}} of HfO₂. The electronic band structure and the corresponding density of states (for the V_{O_{is}} structure) as compared to the pristine slab is presented in Figure 2e. Both V_{O_{is}} and V_{O_{ss}} (see Figure S2 in the SI) led to a decrease of $\sim 0.32 \text{ eV}$ in the bandgap of the pristine slab and the Fermi level is shifted to higher energies confirming the n-type doping effects observed in our experiment. We also observed significant charge transfers (CTs); for example, in the interfacial O-vacancy hybrid structure, our calculations reveal a net charge transfer from the HfO₂ surface to the MoS₂ monolayer of 1.16 |e| ($5.29 \times 10^{13} \text{ e/cm}^2$) per O-vacant site (details in Figures S1d, e and S3 in the SI).

Effect of PEALD Plasma on Bilayer and Trilayer MoS₂ FETs. To gain further understanding of the mechanisms involved in the interface, we extended our study into bilayer and trilayer samples. By examining the effect of ALD and PEALD on bilayer and trilayer MoS₂ FETs, we determined the extent of the plasma damage on the structures. Looking first at the baseline ALD results, we observe that the bilayer and trilayer devices behave similar to monolayer samples showing a negative V_{t} shift and a reduction in hysteresis (Figure 3a and b). Additionally, the PEALD HfO₂ devices behave similarly to the monolayer samples as they exhibit a shift of V_{t} lowering in I_{on} and reduction in hysteresis (Figure 3c and d). However, considering the on-current magnitudes and the transfer characteristics, the bilayer and trilayer PEALD devices show significant improvement over the monolayer devices (Figure 2d). This observation suggests that the plasma interactions occur primarily at the topmost MoS₂ layer. For the monolayer devices, the plasma process degrades most of the channel material and considerably deteriorates the transistor properties. However, for both the bilayer and trilayer samples, the device properties are better preserved since the majority of the sample degradation occurs in the first layer. Since the damage is occurring mostly at the topmost MoS₂ layer, MoS₂ FETs with

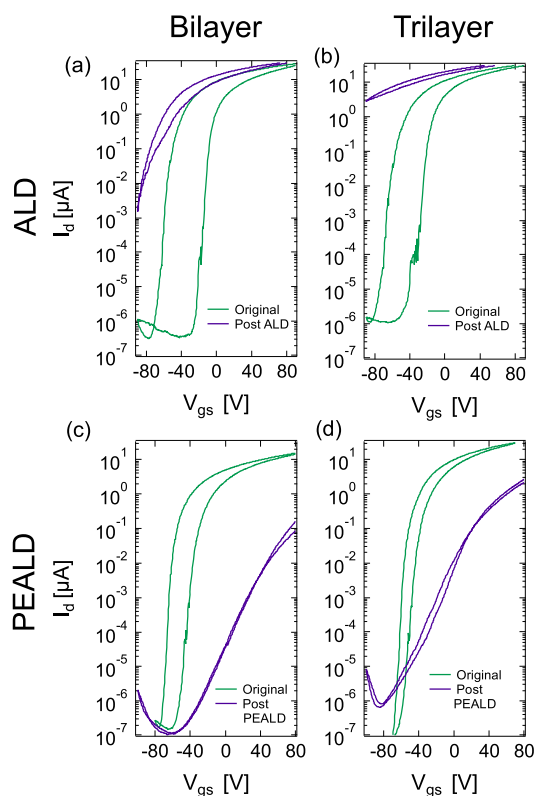


Figure 3. Impact of ALD/PEALD HfO₂ on bilayer and trilayer MoS₂ FETs. Subthreshold curves of (a) bilayer and (b) trilayer MoS₂ FETs before and after ALD 30 nm HfO₂. Subthreshold curves of (c) bilayer and (d) trilayer MoS₂ FETs before and after PEALD HfO₂ ($W = 1.0 \mu\text{m}$, $V_{\text{ds}} = 1.0 \text{ V}$, $L_{\text{ch}} = 0.9 \mu\text{m}$).

a thicker channel are able to retain their electrical performance.²⁷

Raman and PL of PEALD HfO₂ on MoS₂. The electrical measurements demonstrate the impact of the PEALD process on the electrical characteristics of MoS₂ and support the hypothesis that defects can explain these observations. For a more detailed understanding of the role and effects of the plasma-induced defect states on MoS₂, Raman and PL spectroscopy of MoS₂ was carried out. These spectra are strongly affected by the MoS₂ surrounding dielectric environment, strain, defects, and doping.^{37–46} By probing how the PEALD process affects the vibrational and optical properties of MoS₂ via Raman and PL spectroscopy, it was possible to examine the extent of interfacial changes. The symmetry characteristics of MoS₂ allow for four experimentally observable Raman active modes: $34(E_{2g}^2)$, $286(E_{1g})$, $383(E_{2g})$, and $409(A_{1g}) \text{ cm}^{-1}$.⁴⁷ Our measurements focused on the A_{1g} and E_{2g} normal modes, which represent the out-of-plane and in-plane vibrations of the S–Mo–S, respectively. To examine the MoS₂–HfO₂ interface, we performed Raman and PL measurements on our samples before/after ALD/PEALD HfO₂. Focusing on the two main normal modes A_{1g} (out-of-plane vibrations) and E_{2g}^1 (in-plane vibrations), we observed significant changes due to the addition of ALD HfO₂ (Figure 4a and b). In order to accurately compare the spectra before/after ALD/PEALD the peaks were calibrated to the Rayleigh scattering peak.

After ALD HfO₂, the spectra of both monolayer and bilayer MoS₂ samples were blue-shifted with A_{1g} affected more than the E_{2g}^1 mode. The addition of the high- κ dielectric could

influence the MoS₂ Raman spectra in three major ways: the lattice mismatch between the two films can induce strain in the MoS₂ layers, the charge transfer between the two materials can change the electron–phonon scattering, and changes in the dielectric environment can modify the screening properties. All of these effects can modify the bonding properties within MoS₂ and the frequencies of the Raman normal mode. Compressive strain will stiffen the bonds and cause both modes to upshift. However, it is expected for the E_{2g}^1 mode to be affected more than the A_{1g} mode, which does not resemble the trends we observe in our results.^{48,49} Tensile strain should cause the E_{2g}^1 mode to down-shift appreciably while leaving the A_{1g} mode relatively unchanged.⁵⁰ Tensile strain also causes the E_{2g}^1 mode to split for both monolayer and bilayer MoS₂.³⁹ Since our observations do not follow these patterns, we conclude that neither compressive nor tensile strain play a significant role in the changes observed in the Raman spectra for ALD HfO₂–MoS₂. From our transport measurements, we concluded that the ALD HfO₂ is yielding an n-type doping effect on MoS₂ samples, causing changes in the electron densities of the material. If the electron transfer from the ALD-HfO₂ to MoS₂ dominates the interactions, it is expected for the A_{1g} peak would soften and broaden while the E_{2g}^1 mode remains roughly unchanged.^{51,52} As the MoS₂ is doped further (oxygen levels decrease in HfO₂) the shift and broadening of the A_{1g} peak becomes more pronounced.^{53,54} While the Raman spectra changes as the HfO₂ films become more and more oxygen deficient HfO₂, oxygen rich MoS₂ displays very little to no shift in Raman modes.⁵⁵ Other n-type dopants also show the A_{1g} shifting to the left and broadening.^{55,56} In contrast, electron transfer out of the 2D layers should upshift both Raman modes.^{57,58,66} The Raman spectra of a p-type dopant on MoS₂ shows a slight shift to lower values, but the distance between the peaks remains the same.⁵⁹ Stronger p-type dopants have both Raman peaks shifting to the right.⁵⁷ Since the Raman analysis (both peaks shift upward indicating p-type doping) and transport measurements (V_t shift to the left and increase in electron on-current indicating n-type doping) are contradictory, we conclude that doping is not the cause of the Raman peaks shift, instead another factor must be considered. One factor to consider is the change in the dielectric environment—going from air to high- κ . This increase in the dielectric screening of the stacked HfO₂–MoS₂ should stiffen the bonds and upshift both peaks. The pattern of our results suggests that this is the dominant effect resulting in the uniform upshift of both normal-mode frequencies of the pristine ALD HfO₂–MoS₂.

The Raman spectra acquired from the PEALD HfO₂–MoS₂ stacks suggest a significant change in the interface properties. These effects in the monolayer samples include the rise and disappearance of peaks and changes in peak positions and line width of the normal modes relative to the reference samples (Figure 4c and d). To explain the observed effects, we need a better understanding of the phonon dispersion characteristics and the role of defects in MoS₂.⁶⁰ Defects perturb the spatial translational invariance of crystalline structures resulting in finite phonon correlation length. These phonon confinement effects breakdown the selection rules; allowing new phonon peaks to arise and the first order Raman peaks to shift and broaden.⁶¹ The effects of these changes on the Raman spectra can be explained by the phonon confinement model.⁵¹ The theory suggests that the shift in the normal peak positions as a function of the density of defects should resemble the phonon

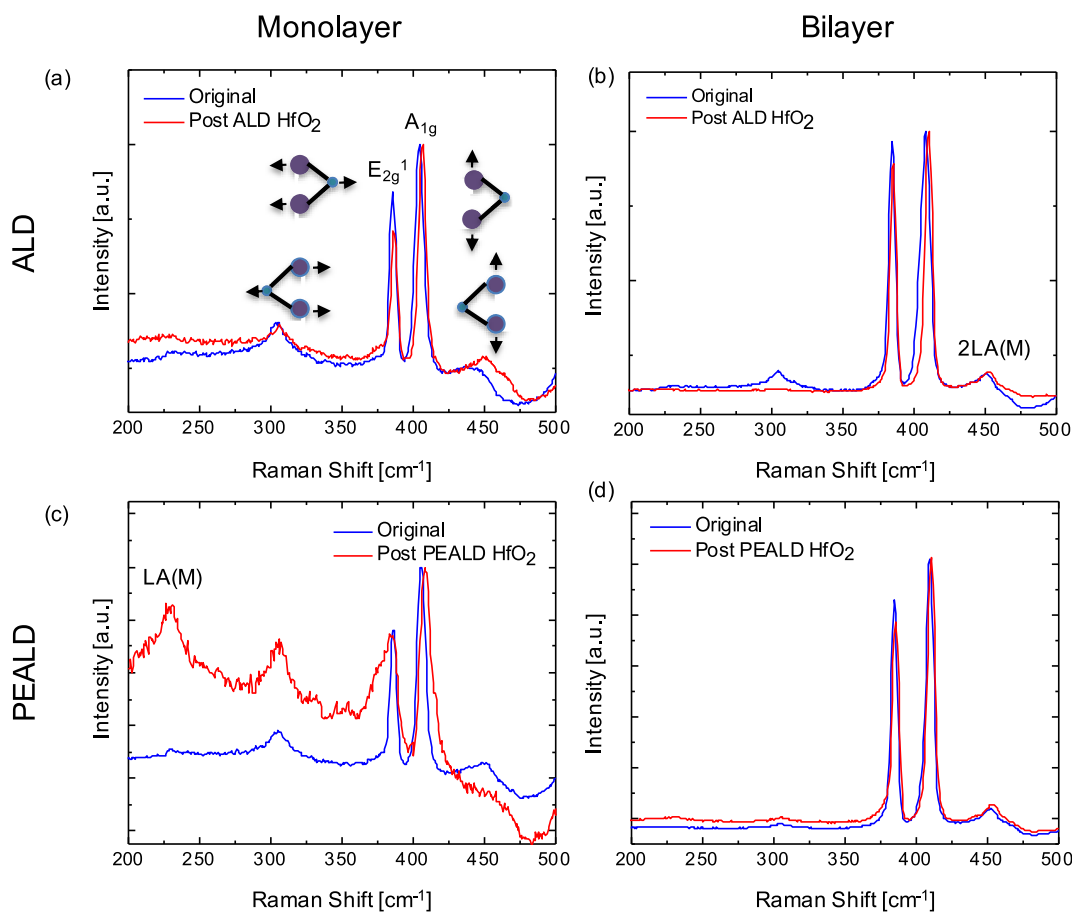


Figure 4. Raman spectroscopy analysis of ALD and PEALD effects on monolayer versus bilayer MoS₂. Raman spectra (measured at liquid nitrogen temperatures and under high vacuum) of (a) monolayer and (b) bilayer MoS₂ before/after ALD HfO₂. Raman spectra of (c) monolayer and (d) bilayer MoS₂ before/after PEALD HfO₂.

dispersion of each branch moving away from the Γ point. Looking at the phonon dispersion curves of MoS₂, from the center of the Brillouin zone, we expect that as the density of defects increases, the frequency of the ZO phonon branch will increase whereas the LO and TO phonon branches should decrease. The broadening of the E_{2g}¹ Raman modes and appearance of new peaks is expected due to the defect-activated mechanism. The E_{2g}¹ peak should split into the LO(SP), LO(M), and TO(M) peaks near the A_{1g} peak, an additional ZO(M) peak should also arise.^{61,62}

The shift and broadening of the normal modes in our experiments follow the predictions of the phonon confinement model for MoS₂ in the presence of defects, with slight changes due to the dielectric screening effects in the high-dielectric stacks (Figure 4c and d). In addition, observing the defect-mediated longitudinal acoustic LA(M) mode at 228 cm⁻¹ further confirms the formation of defects in MoS₂. This peak is a signature of disorder in MoS₂, and its intensity has been correlated to the density of defects.^{63–65} The more commonly observed, second order peak related to this branch of acoustic modes, 2LA(M), is absent in the spectra, most likely due to the significant rise in the lattice distortions in the material after PEALD processing.⁴⁴ In comparison, a distinct behavior can be seen in bilayer MoS₂ where the PEALD HfO₂ resulted in a blue-shift of both Raman modes—similar to post ALD HfO₂ on monolayer and bilayer MoS₂. Therefore, we conclude that monolayer samples sustain significantly more damage at the interface as compared to bilayer samples. However, what is not

clear in these observations is the possible charge transfer characteristics of the stacked system.

For more insight into the charge transfer in the HfO₂–MoS₂ heterostructures, we performed PL measurements on monolayer and bilayer CVD-grown MoS₂. Bulk MoS₂ is an indirect bandgap semiconductor with a small radiative emission. However, the transition into a direct bandgap semiconductor for monolayer MoS₂ allows for the observation of strong PL emission peaks.⁶⁶ The MoS₂ PL spectra includes two sharp emission peaks, namely A (665 nm) and B (615 nm), corresponding to the excitonic transition from the spin–orbit split of two valence band edges to the bottom of the conduction band.^{67,68} Additionally, the changes in the electron doping levels in MoS₂ can lead to clear changes in the characteristic PL emission spectra. The two-dimensional nature of MoS₂ and the screening effects generally lead to strong binding energies and the appearance of charged excitons, namely negatively charged trions (A⁻). The PL spectrum in MoS₂ has therefore shown strong sensitivity to doping levels. As electron concentrations change in MoS₂, the trion population changes and results in modification of the PL intensity.^{38,41,46,69} These effects appear in the PL spectra of the material in the form of changes in the intensity of the shoulder near the A peak. By fitting the PL peaks and quantifying the underlying emission properties, one can extract a detailed understanding of the underlying mechanisms of interactions involved (Figure 5).

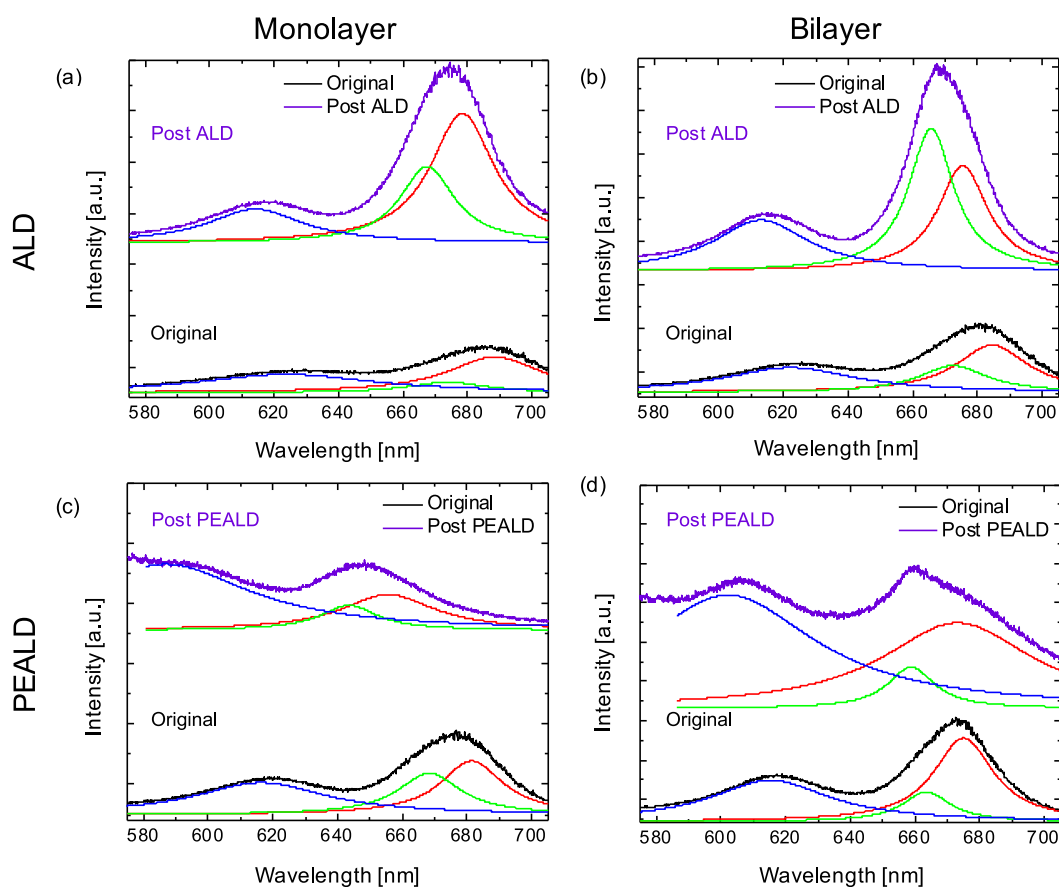


Figure 5. Photoluminescence analysis of ALD and PEALD effects on monolayer versus bilayer MoS₂ under vacuum at liquid N₂ temperature. Photoluminescence of monolayer/bilayer MoS₂ after the deposition of (a/c) ALD or (b/d) PEALD HfO₂. The peaks are fitted using Gaussian fitting parameters; the blue lines represent the B exciton, the green line is the A exciton, and the red line is the trion.

We measured the PL spectra of ALD HfO₂–MoS₂ samples to determine the reference interactions between the pristine interfaces of the dielectric and the 2D material. Our PL measurements on these samples show a noteworthy blue-shift and a strong increase in the PL intensity of both monolayer and bilayers after ALD of HfO₂ (Figure 4a and b). These results are somewhat contradictory. If MoS₂ was becoming more electron rich, one would expect an upward shift, decrease in intensity, and a rise in the trion peak.⁵⁵ As HfO₂ becomes more oxygen deficient, the PL decreases in intensity and shifts increasingly more.⁵⁴ After ALD, the PL results show a redshift, increase in intensity, and rise in the trion peak. Since the PL measurements do not follow all of the requirements to exhibit n-type doping, other factors that could influence the PL spectra must be considered. One such factor, is the change in the dielectric environment as the high- κ dielectric oxide replaces vacuum. Consistent with the Raman measurement, the dominant interaction between the ALD HfO₂ and MoS₂ is the stiffening of the bonds (the blue-shift in PL and Raman) and changes in the dielectric shielding. The resultant influence of these changes on the binding energy of excitons describes the strong increase in the intensity of the emission peaks (Figure 5a and b). In addition to these changes, a rise in a shoulder peak (A⁻ peak) is clearly discernible and is attributed to the changes in electron concentration levels in the material. The dielectric in contact with MoS₂ can exchange charge and dope MoS₂ (either making it electron-rich or -deficient). Even though our results do not exhibit all of the characteristics

associated with electron doping, the increase of the trion peak (A⁻) does indicate that there is a transfer of electrons from HfO₂ to MoS₂. Based on our results, we conclude that there is a stiffening of the bonds, change in dielectric shielding, and a charge transfer from the HfO₂ to MoS₂ in the stacked structure in both monolayer and bilayer samples.

The PL emissions from the post-PEALD HfO₂ monolayer MoS₂ show contrasting behavior when compared to the ALD HfO₂ stacks. Although there is a PL blue-shift because of the dielectric changes in the environment, which resembles the blue-shift of the ALD stacks, the intensity decreases substantially and the ratio of B to A excitons increases. The most likely reason for this change is defect formations in MoS₂, as was previously confirmed in our Raman studies of Figure 3. Defects in MoS₂ have been shown to significantly reduce the PL intensity, which we observe in the case of PEALD HfO₂.^{43,44,61} Additionally, we observe a rise in the A⁻ trion peaks, which also suggest that there is a charge transfer from HfO₂ to MoS₂. A similar trend in the bilayer samples is also observed, suggesting that while defect formation is inherent to the plasma-enhanced process, a charge transfer from the oxides to the 2D system ensues. However, only a direct analysis of the defects and their role can validate the spectroscopic evidence.

TEM of Trilayer MoS₂ Post PEALD HfO₂. To further study the defects at the interface of PEALD and MoS₂, we employed scanning transmission electron microscopy (STEM) and high-resolution transmission electron microscopy (HRTEM) to examine the trilayer MoS₂ samples (Figure 5a

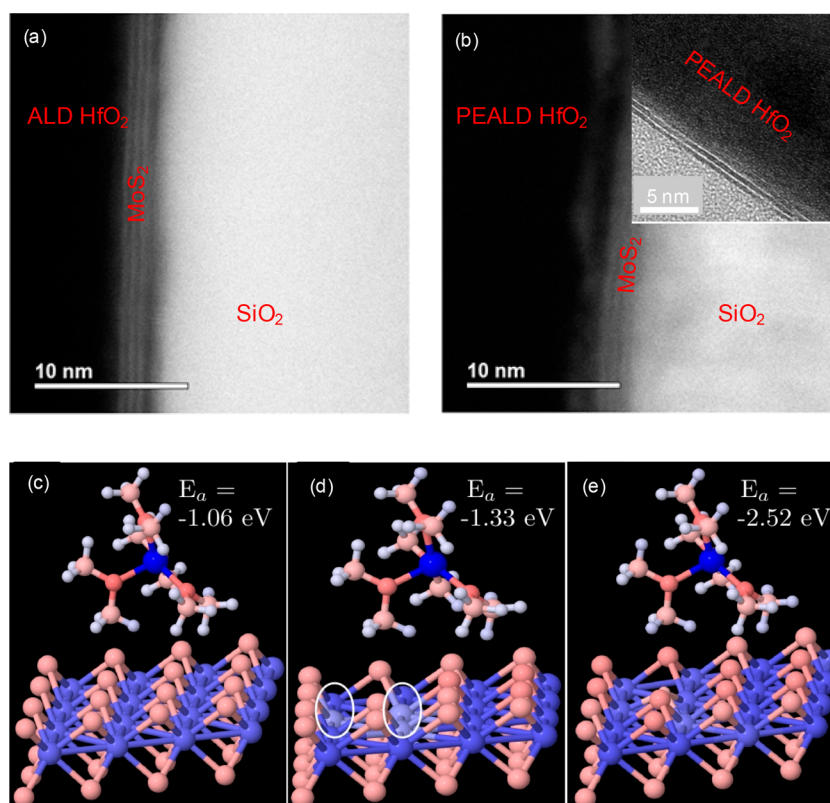


Figure 6. STEM and HRTEM (inset) images of trilayer MoS₂ after (a) ALD and (b) PEALD HfO₂. The calculated binding energy of TDMAH to (c) pristine MoS₂, (d) sulfur vacancies, and (e) hydrogen-passivated sulfur vacancies is shown.

and b). In the case of ALD HfO₂, the STEM (Figure 6a) image indicates little or no damage to the MoS₂ sample and the three MoS₂ layers can be perfectly distinguished. This is expected as the ALD process causes insignificant damage to MoS₂ samples as it grows by physical adsorption or via naturally occurring defect sites.¹⁴ However, the PEALD HfO₂ samples show very different interfacial properties (Figure 6b) where three MoS₂ layers are visible, but they are blurry and indistinct indicating possible damage. By imaging further using HRTEM, it becomes evident that there are two distinct MoS₂ layers and a third (topmost) blurry layer (Figure 5b inset). The results strongly support our electrical and spectroscopic measurements and suggest that the PEALD process induces substantial damage to the topmost MoS₂ layer. The consistent evidence of damage at the topmost layer of PEALD samples is at times complemented in some regions with extensive damage and total amorphization of MoS₂ extending into all of the layers. While these results give a more complete picture of the interfaces, they also emphasize the need for further process development for optimization of the PEALD process in order to scale the gate dielectric. To guide these future efforts, we need a theoretical understanding of the role of defects in the nucleation and growth of ALD materials. The most energetic orientation of the TDMAH precursor on MoS₂ is determined using the nudged elastic band method. We calculated the adsorption energy for three different scenarios of an ALD precursor on MoS₂. We examined TDMAH energetics on pristine MoS₂ (Figure 6c), at sulfur vacancies within MoS₂ (Figure 6d), and with hydrogen-passivated sulfur vacancies (Figure 6e) (see also Figures S3–S6 in the SI). It is clear from our results that the hydrogen-passivated vacancies in MoS₂ have the lowest adsorption energy and, as such, are the most

chemically stable, meaning that the defect formations in the plasma-enhanced process most likely promote material nucleation and growth in the ALD reaction and are a necessary component of the dielectric growth. This makes the device characteristics in monolayer MoS₂ and dielectric thickness scaling two competing properties.

CONCLUSION

In summary, we have explored the impact of the PEALD process on monolayer, bilayer, and trilayer MoS₂. We used electrical measurements, Raman spectroscopy, PL, TEM imaging, and first-principles calculations to provide a detailed understanding of the device interfaces and the role of plasma in PEALD HfO₂ on MoS₂. It is evident from our spectroscopic studies and TEM imaging of the interfaces that the PEALD process leads to significant damage to the monolayer samples. These effects combined with the charge transfer properties inherent to the substoichiometric HfO₂ constitute the changes at the PEALD HfO₂–MoS₂ interface. Even though the damage due to defects in the crystal structure of MoS₂ promotes ALD growth and enables dielectric thickness scaling, it also substantially degrades the device performance for MoS₂ of a few layers or less. However, our results suggest that this damage at the interfaces is incurred primarily at the topmost layers and when the thickness of the 2D layers is scaled up, the deterioration of the device performance is greatly reduced. These results unveil a competing relationship between the dielectric thickness scaling, 2D material thickness scaling, and device electrical properties that stem from the inertness of the surface of 2D materials. These observations present a deeper understanding of the role of the plasma process on MoS₂ in

device processing and provide a guideline for the integration of high- κ dielectrics onto 2D crystals.

■ ASSOCIATED CONTENT

Supporting Information

The Supporting Information is available free of charge on the ACS Publications website at DOI: 10.1021/acsanm.9b00505.

Figures S1–S8 as mentioned in the text (PDF)

■ AUTHOR INFORMATION

Corresponding Author

*Email: aaron.franklin@duke.edu.

ORCID

Katherine M. Price: 0000-0001-6120-0020

Chinedu E. Ekuma: 0000-0002-5852-7556

Aaron D. Franklin: 0000-0002-1128-9327

Notes

The authors declare no competing financial interest.

■ ACKNOWLEDGMENTS

The research was sponsored by the Army Research Laboratory (ARL) and was accomplished under the Cooperative Agreement No. W911NF-11-2-0030 as an ARL Research [George F. Adams] Fellow. Supercomputer support is provided by the DOD High-Performance Computing Modernization Program at the Army Engineer Research and Development Center, Vicksburg, MS.

■ REFERENCES

- (1) Radisavljevic, B.; Radenovic, A.; Brivio, J.; Giacometti, V.; Kis, A. Single-layer MoS₂ transistors. *Nat. Nanotechnol.* **2011**, *6*, 147–150.
- (2) Das, S.; Chen, H. Y.; Penumatcha, A. V.; Appenzeller, J. High performance multilayer MoS₂ transistors with scandium contacts. *Nano Lett.* **2013**, *13*, 100–105.
- (3) Wang, H.; Yu, L.; Lee, Y.; Shi, Y.; Hsu, A.; Chin, M.; Li, L.; Dubey, M.; Kong, J.; Palacios, T. Integrated Circuits Based on Bilayer MoS₂ Transistors. *Nano Lett.* **2012**, *12*, 4674–4680.
- (4) Radisavljevic, B.; Whitwick, M. B.; Kis, A. Small-signal amplifier based on single-layer MoS₂. *Appl. Phys. Lett.* **2012**, *101*, 043103.
- (5) Zhang, W.; Huang, J.; Chen, C.; Chang, Y.; Cheng, Y.; Li, L. High-gain phototransistors based on a CVD MoS₂ monolayer. *Adv. Mater.* **2013**, *25*, 3456–3461.
- (6) Lee, H. S.; Min, S.; Chang, Y.; Park, M.; Nam, T.; Kim, H.; Kim, J.; Ryu, S.; Im, S. MoS₂ Nanosheet Phototransistors with Thickness-Modulated Optical Energy Gap. *Nano Lett.* **2012**, *12*, 3695–3700.
- (7) Dickinson, R. G.; Pauling, L. The crystal structure of molybdenite. *J. Am. Chem. Soc.* **1923**, *45*, 1466–1471.
- (8) Novoselov, A. K. S.; Jiang, D.; Schedin, F.; Booth, T.; Khotkevich, V.; Morozov, S.; Geim, A.; Rice, T. Two-dimensional atomic crystals. *Proc. Natl. Acad. Sci. U. S. A.* **2005**, *102*, 10451–10453.
- (9) Late, D. J.; Liu, B.; Matte, H. S. S. R.; Dravid, V. P.; Rao, C. N. R. Hysteresis in single-layer MoS₂ field effect transistors. *ACS Nano* **2012**, *6*, 5635–41.
- (10) Park, W.; Park, J.; Jang, J.; Lee, H.; Jeong, H.; Cho, K.; Hong, S.; Lee, T. Oxygen environmental and passivation effects on molybdenum disulfide field effect transistors. *Nanotechnology* **2013**, *24*, 095202.
- (11) Qiu, H.; Pan, L.; Yao, Z.; Li, J.; Shi, Y.; Wang, X. Electrical characterization of back-gated bi-layer MoS₂ field-effect transistors and the effect of ambient on their performances. *Appl. Phys. Lett.* **2012**, *100*, 123104.
- (12) George, S. M. Atomic Layer Deposition: An Overview. *Chem. Rev.* **2010**, *110*, 111–131.
- (13) Liu, H.; Xu, K.; Zhang, X.; Ye, P. D. The integration of high- κ dielectric on two-dimensional crystals by atomic layer deposition. *Appl. Phys. Lett.* **2012**, *100*, 152115.
- (14) McDonnell, S.; Brennan, B.; Azcatl, A.; Lu, N.; Dong, H.; Buie, C.; Kim, J.; Hinkle, C.; Kim, M.; Wallace, R. HfO₂ on MoS₂ by atomic layer deposition: Adsorption mechanisms and thickness scalability. *ACS Nano* **2013**, *7*, 10354–10361.
- (15) Liu, H.; Ye, P. D. MoS₂ dual-gate MOSFET with atomic-layer-deposited Al₂O₃ as top-gate dielectric. *IEEE Electron Device Lett.* **2012**, *33*, 546–548.
- (16) Son, S.; Yu, S.; Choi, M.; Kim, D.; Choi, C. Improved high temperature integration of Al₂O₃ on MoS₂ by using a metal oxide buffer layer. *Appl. Phys. Lett.* **2015**, *106*, 021601.
- (17) Qian, Q.; Zhang, Z.; Hua, M.; Tang, G.; Lei, J.; Lan, F.; Xu, Y.; Yan, R.; Chen, K. Enhanced dielectric deposition on single-layer MoS₂ with low damage using remote N₂ plasma treatment. *Nanotechnology* **2017**, *28*, 175202.
- (18) Nourbakhsh, A.; Adelman, C.; Song, Y.; Lee, C.; Asselberghs, I.; Huygebaert, C.; Brizzi, S.; Tallarida, M.; Schmeiber, D.; Elshocht, S.; Heyns, M.; Kong, J.; Palacios, T.; De Gendt, S. Graphene oxide monolayers as atomically thin seeding layers for atomic layer deposition of metal oxides. *Nanoscale* **2015**, *7*, 10781–10789.
- (19) Azcatl, A.; McDonnell, S.; K. C. S.; Peng, X.; Dong, H.; Qin, X.; Addou, R.; Mordi, G. I.; Lu, N.; Kim, J.; Kim, M. J.; Cho, K.; Wallace, R. M. MoS₂ functionalization for ultra-thin atomic layer deposited dielectrics. *Appl. Phys. Lett.* **2014**, *104*, 111601.
- (20) Le, Q. V.; Nguyen, T. P.; Jang, H. W.; Kim, S. Y. The use of UV/ozone-treated MoS₂ nanosheets for extended air stability in organic photovoltaic cells. *Phys. Chem. Chem. Phys.* **2014**, *16*, 13123.
- (21) Lim, T.; Kim, D.; Ju, S. Nitrogen plasma treatment Direct deposition of aluminum oxide gate dielectric on graphene channel using nitrogen plasma treatment. *Appl. Phys. Lett.* **2013**, *103*, 013107.
- (22) Yang, W.; Sun, Q.; Geng, Y.; Chen, L.; Zhou, P.; Ding, S.; Zhang, D. The Integration of Sub-10 nm Gate Oxide on MoS₂ with Ultra Low Leakage and Enhanced Mobility. *Sci. Rep.* **2015**, *5*, 11921.
- (23) Lee, B.; Park, S.; Kim, H.; Cho, K.; Vogel, E.; Kim, M.; Wallace, R.; Kim, J. Conformal Al₂O₃ dielectric layer deposited by atomic layer deposition for graphene-based nanoelectronics. *Appl. Phys. Lett.* **2008**, *92*, 203102.
- (24) Park, S.; Kim, S.; Choi, Y.; Kim, M.; Shin, H.; Kim, J.; Choi, W. Interface Properties of Atomic-Layer-Deposited Al₂O₃ Thin Films on Ultraviolet/Ozone-Treated Multilayer MoS₂ Crystals. *ACS Appl. Mater. Interfaces* **2016**, *8*, 11189–11193.
- (25) Alaboson, J. M. P.; Wang, Q.; Emery, J.; Lipson, A.; Bedzyk, M.; Elam, J.; Pellin, M.; Hersam, M. Seeding atomic layer deposition of high- κ dielectrics on epitaxial graphene with organic self-assembled monolayers. *ACS Nano* **2011**, *5*, 5223–5232.
- (26) Yang, J.; Kim, S.; Choi, W.; Park, S.; Jung, Y.; Cho, M.; Kim, H. Improved growth behavior of atomic-layer-deposited high- κ dielectrics on multilayer MoS₂ by oxygen plasma pretreatment. *ACS Appl. Mater. Interfaces* **2013**, *5*, 4739–4744.
- (27) Price, K. M.; Schauble, K. E.; McGuire, F. A.; Farmer, D. B.; Franklin, A. D. Uniform Growth of Sub-5-Nanometer High- κ Dielectrics on MoS₂ Using Plasma-Enhanced Atomic Layer Deposition. *ACS Appl. Mater. Interfaces* **2017**, *9*, 23072–23080.
- (28) Hohenberg, P.; Kohn, W. Inhomogeneous Electron Gas. *Phys. Rev.* **1964**, *136*, B864–B871.
- (29) Kresse, G.; Furthmüller, J. Efficiency of ab-initio total energy calculations for metals and semiconductors using a plane-wave basis set. *Comput. Mater. Sci.* **1996**, *6*, 15–50.
- (30) Cheng, Z.; Price, K.; Franklin, A. Contacting and Gating 2-D Nanomaterials. *IEEE Trans. Electron Devices* **2018**, *65*, 4073–4083.
- (31) Li, S.-L.; Wakabayashi, K.; Xu, Y.; Nakaharai, S.; Komatsu, K.; Li, W.; Lin, Y.; Aparcedio-Ferreira, A.; Tsukagoshi, K. Thickness-Dependent Interfacial Coulomb Scattering in Atomically Thin Field-Effect Transistors. *Nano Lett.* **2013**, *13*, 3546.
- (32) Profijt, H. B.; Potts, S. E.; van de Sanden, M. C. M.; Kessels, W. M. M. Plasma-Assisted Atomic Layer Deposition: Basics, Opportunities, and Challenges. *J. Vac. Sci. Technol., A* **2011**, *29*, 050801.

- (33) Rai, A.; Valsaraj, A.; Movva, H.; Roy, A.; Tutuc, R.; Register, L.; Banerjee, S. Interfacial-Oxygen-Vacancy Mediated Doping of MoS₂ by High-K Dielectrics. *IEEE Device Res. Conf.* **2015**, 189–190.
- (34) Zhu, W. J.; Ma, T. P.; Zafar, S.; Tamagawa, T. *IEEE Electron Device Lett.* **2002**, *23*, 597–599.
- (35) Wang, J.; Sadegh Mottaghian, S.; Farrokh Baroughi, M. Passivation properties of atomic-layer-deposited hafnium and aluminum oxides on Si surfaces. *IEEE Trans. Electron Devices* **2012**, *59*, 342–348.
- (36) Sreenivasan, R.; McIntyre, P. C.; Kim, H.; Saraswat, K. C. Effect of impurities on the fixed charge of nanoscale films grown by atomic layer deposition H-related defect complexes in A model for positive fixed charge defects Effect of impurities on the fixed charge of nanoscale HfO₂ films grown by atomic layer deposition. *Appl. Phys. Lett.* **2006**, *89*, 112903–121301.
- (37) Lin, Y.; Ling, X.; Yu, L.; Huang, S.; Hsu, A.; Lee, Y.; Kong, J.; Dresselhaus, M.; Palacios, T. Dielectric Screening of Excitons and Trions in Single-Layer MoS. *Nano Lett.* **2014**, *14*, 5569.
- (38) Mak, K. F.; He, K.; Lee, C.; Lee, G.; Hone, J.; Heinz, T.; Shan, J. Tightly bound trions in monolayer MoS₂. *Nat. Mater.* **2013**, *12*, 207–211.
- (39) Zhu, C. R.; Wang, G.; Liu, B.; Marie, X.; Qiao, X.; Zhang, X.; Wu, X.; Fan, H.; Tan, P.; Amand, T.; Urbaszek, B. Strain tuning of optical emission energy and polarization in monolayer and bilayer MoS₂. *Phys. Rev. B: Condens. Matter Mater. Phys.* **2013**, *88*, 121301.
- (40) Nan, H.; Wang, Z.; Wang, W.; Liang, Z.; Lu, Y.; Chen, Q.; He, D.; Tan, P.; Miao, F.; Wang, X.; Wang, J.; Ni, Z. Strong photoluminescence enhancement of MoS₂ through defect engineering and oxygen bonding. *ACS Nano* **2014**, *8*, 5738–5745.
- (41) Mouri, S.; Miyauchi, Y.; Matsuda, K. Tunable Photoluminescence of Monolayer MoS₂ via Chemical Doping. *Nano Lett.* **2013**, *13*, 5944–5948.
- (42) Chow, P. K.; Jacobs-Gedrim, R.; Gao, J.; Lu, T.; Yu, B.; Terrones, H.; Koratkar, N. Defect-induced photoluminescence in monolayer semiconducting transition metal dichalcogenides. *ACS Nano* **2015**, *9*, 1520–1527.
- (43) Tongay, S.; Suh, J.; Ataca, C.; Fan, W.; Luce, A.; Kang, J.; Liu, J.; Ko, C.; Raghunathanan, R.; Zhou, J.; Ogletree, F.; Li, J.; Grossman, J.; Wu, J. Defects activated photoluminescence in two-dimensional semiconductors: interplay between bound, charged and free excitons. *Sci. Rep.* **2013**, *3*, 2657.
- (44) Kang, N.; Paudel, H. P.; Leuenberger, M. N.; Tetard, L.; Khondaker, S. I. Photoluminescence Quenching in Single-Layer MoS₂ via Oxygen Plasma Treatment. *J. Phys. Chem. C* **2014**, *118*, 21258–21263.
- (45) Conley, H. J.; Wang, B.; Ziegler, J.; Haglund, R.; Pantelides, S.; Bolotin, K. Bandgap Engineering of Strained Monolayer and Bilayer MoS₂. *Nano Lett.* **2013**, *13*, 3626–3630.
- (46) Yan, R.; Bertalazzi, S.; Brivio, J.; Fang, T.; Konar, A.; Birdwell, A.; Nguyen, N.; Kis, A.; Jena, D.; Xing, H. Raman and Photoluminescence Study of Dielectric and Thermal Effects on Atomically Thin MoS₂. *arXiv.org* **2012**, *17*, 1211.4136.
- (47) Wieting, T. J.; Verble, J. L. Infrared and Raman studies of long-wavelength optical phonons in hexagonal MoS₂. *Phys. Rev. B* **1971**, *3*, 4286.
- (48) Scalise, E.; Houssa, M.; Pourtois, G.; Afanasev, V. V.; Stesmans, A. First-principles study of strained 2D MoS₂. *Phys. E* **2014**, *56*, 416–421.
- (49) Rice, C.; Young, R. J.; Zan, R.; Bangert, U.; et al. Raman-scattering measurements and first-principles calculations of strain-induced phonon shifts in monolayer MoS₂. *Phys. Rev. B: Condens. Matter Mater. Phys.* **2013**, *87*, 1–5.
- (50) Wang, Y.; Cong, C.; Qiu, C.; Yu, T. Raman spectroscopy study of lattice vibration and crystallographic orientation of monolayer MoS₂ under uniaxial strain. *Small* **2013**, *9*, 2857–2861.
- (51) Chakraborty, B.; Bera, A.; Muthu, D.; Bhowmick, S.; Waghmare, U.; Sood, A. Symmetry-dependent phonon renormalization in monolayer MoS₂ transistor. *Phys. Rev. B: Condens. Matter Mater. Phys.* **2012**, *85*, 161403.
- (52) Rai, A.; Valsaraj, A.; Movva, H.; Roy, A.; Ghosh, R.; Sonde, S.; Kang, S.; Chang, J.; Trivedi, T.; Dey, R.; Guchhait, S.; Larentis, S.; Register, L.; Tutuc, E.; Banerjee, S. Air Stable Doping and Intrinsic Mobility Enhancement in Monolayer Molybdenum Disulfide by Amorphous Titanium Suboxide Encapsulation. *Nano Lett.* **2015**, *15*, 4329–4336.
- (53) Alharbi, A.; Shahrjerdi, D. Analyzing the Effect of High-k Dielectric-Mediated Doping on Contact Resistance in Top-Gated Monolayer MoS₂ Transistors. *IEEE Trans. Electron Devices* **2018**, *65*, 4084–4092.
- (54) Alharbi, A.; Shahrjerdi, D. Contact engineering of monolayer CVD MOS₂ transistors. *Device Res. Conf.–Conf. Dig. DRC*; 2017; Vol. 15.
- (55) Kiriya, D.; Tosun, M.; Zhao, P.; Kang, J. S.; Javey, A. Air-stable surface charge transfer doping of MoS₂ by benzyl viologen. *J. Am. Chem. Soc.* **2014**, *136*, 7853–7856.
- (56) Lockhart De La Rosa, C. J.; Nourbakhsh, A.; Heyne, M.; Asselberghs, I.; Huygebaert, C.; Radu, I.; Heyns, M.; de Gendt, S. Highly efficient and stable MoS₂ FETs with reversible n-doping using a dehydrated poly(vinyl-alcohol) coating. *Nanoscale* **2017**, *9*, 258–265.
- (57) Tarasov, A.; Zhang, S.; Tsai, M.; Campbell, P.; Graham, S.; Barlow, S.; Marder, S.; Vogel, E. Controlled doping of large-area trilayer MoS₂ with molecular reductants and oxidants. *Adv. Mater.* **2015**, *27*, 1175–1181.
- (58) Kiriya, D.; Tosun, M.; Zhao, P.; Kang, J. S.; Javey, A. Air-stable surface charge transfer doping of MoS₂ by benzyl viologen. *J. Am. Chem. Soc.* **2014**, *136*, 7853–6.
- (59) Min, S. W.; Yoon, M.; Yang, S. J.; Ko, K. R.; Im, S. Charge-Transfer-Induced p-Type Channel in MoS₂ Flake Field Effect Transistors. *ACS Appl. Mater. Interfaces* **2018**, *10*, 4206–4212.
- (60) Richter, H.; Wang, Z. P.; Ley, L. THE ONE PHONON RAMAN SPECTRUM IN MICROCRYSTALLINE SILICON. *Solid State Commun.* **1981**, *39*, 625–629.
- (61) Zhang, X.; Qiao, X.; Shi, W.; Wu, J.; Jiang, D.; Tan, P. Phonon and Raman scattering of two-dimensional transition metal dichalcogenides from monolayer, multilayer to bulk material. *Chem. Soc. Rev.* **2015**, *44*, 2757–2785.
- (62) Shi, W.; Lin, M.-L.; Tan, Q.-H. Raman and photoluminescence spectra of two-dimensional nanocrystallites of monolayer WS₂ and WSe₂. *2D Mater.* **2016**, *3* (2), 025016.
- (63) Sourisseau, C.; Cruge, F.; Fouassier, M.; Alba, M. Second-order Raman effects, inelastic neutron scattering and lattice dynamics in 2H-WS₂. *Chem. Phys.* **1991**, *150*, 281–293.
- (64) Mignuzzi, S.; Pollard, A.; Bonini, N.; Brennan, B.; Gilmore, I.; Pimenta, M.; Richards, D.; Roy, D. Effect of disorder on Raman scattering of single-layer MoS₂. *Phys. Rev. B: Condens. Matter Mater. Phys.* **2015**, *91*, 195411.
- (65) Frey, G. L.; Tenne, R.; Matthews, M. J.; Dresselhaus, M. S.; Dresselhaus, G. Raman and resonance Raman investigation of MoS₂ nanoparticles. *Phys. Rev. B: Condens. Matter Mater. Phys.* **1999**, *60*, 2883–2892.
- (66) Splendiani, A.; Sun, L.; Zhang, Y.; Li, T.; Kim, J.; Chim, C.; Galli, G.; Wang, F. Emerging Photoluminescence in Monolayer MoS₂. *Nano Lett.* **2010**, *10*, 1271–1275.
- (67) Coehoorn, R.; Haas, C.; Dijkstra, J.; Flipse, C.; de Groot, R.; Wold, A. Electronic structure of MoSe₂, MoS₂, and WSe₂. I. Band-structure calculations and photoelectron spectroscopy. *Phys. Rev. B: Condens. Matter Mater. Phys.* **1987**, *35*, 6195–6202.
- (68) Coehoorn, R.; Haas, C.; De Groot, R. A. Electronic structure of MoSe₂, MoS₂, and WSe₂. II. The nature of the optical band gaps. *Phys. Rev. B: Condens. Matter Mater. Phys.* **1987**, *35*, 6203–6206.
- (69) Sercombe, D.; Schwarz, S.; Del Pozo-Zamudio, O.; Liu, F.; Robinson, B.; Chekhovich, E.; Tartakovskii, I.; Kolosov, O.; Tartakovskii, A. Optical investigation of the natural electron doping in thin MoS₂ films deposited on dielectric substrates. *Sci. Rep.* **2013**, DOI: 10.1038/srep03489.